ADVANCED MATERIALS
www.advmat.de

Topologically Protected Quantum Logic Gates with Valley-Hall Photonic Crystals

Lu He, Dongning Liu, Huizhen Zhang, Furong Zhang, Weixuan Zhang, Xue Feng, Yidong Huang, Kaiyu Cui, Fang Liu, Wei Zhang, and Xiangdong Zhang**

Topological photonics provide a promising way to realize more robust optical devices against some defects and environmental perturbations. Quantum logic gates are fundamental units of quantum computers, which are widely used in future quantum information processing. Thus, constructing robust universal quantum logic gates is an important way forward to practical quantum computing. However, the most important problem to be solved is how to construct the quantum-logic-gate-required 2 × 2 beam splitter with topological protection. Here, the experimental realization of the topologically protected contradirectional coupler is reported, which can be employed to realize the quantum logic gates, including control-NOT and Hadamard gates, on the silicon photonic platform. These quantum gates not only have high experimental fidelities but also exhibit a certain degree of tolerances against certain types of defects. This work paves the way for the development of practical optical quantum computations and signal processing.

1. Introduction

The integrated quantum gate is an essential part to realize the universal quantum computer, which is capable of simulating any physical system and represents a major goal for the field of quantum information science.[1] The quantum computer[2] can be created by constructing networks of quantum operators in universal gate sets,[3–6] which include the controlled-NOT (CNOT) gate[7–21] and single-qubit gates.[22] Quantum photonic integrated circuits with CNOT gates and Hadamard gates are well recognized as the attractive technology offering a great promise for achieving large-scale quantum information processing.[23–26] For practical applications of the universal quantum computer, we need to implement quantum circuits with as many qubits as possible and enhance their robustness against various types of errors and noises.[27] To solve such a problem, the quantum error correction method[28–36] is first considered and introduced into the study of quantum computing. However, such a scheme is extremely difficult to implement because it requires a lot of additional resource consumptions of quantum circuits. Another important problem is how to construct robust quantum logic devices in chips, which can be against a certain degree of manufacturing defects. By constructing a robust quantum circuit, especially robust quantum gates, some manufacturing defects can be well ignored. However, how to construct robust quantum logic devices in chips, which can against a certain degree of manufacturing defects, is always an open problem.

On the other hand, topological photonics have increasingly received much attentions in the past few years.[37–53] The unique robust edge state displays lots of novel phenomena with unidirectional and defect-immune propagating. In recent studies, various topological photonic structures are demonstrated in the frequency range of microwave,[39,40,45] terahertz,[50,51] and near-infrared,[46,48,49] regions. These topological devices possess a certain degree of robustness[54,55] than those based on the traditional optical platform, which shows a good performance against the 60° and 120° waveguide bending defects. All these studies about topological photonics have been focused on classical electromagnetic systems. It is increasingly curious about what would happen if topological photonics were used to protect quantum states.[56–64] Recently, the topological protection of biphoton states,[57] valley-dependent quantum photonic circuits,[60–63] and on-chip polarization quantum entanglements[64] have been experimentally demonstrated. Furthermore, if topologically protected quantum gates can be constructed, it is expected that the large-scale topologically protected quantum circuit against some defects can be realized. However, it is not easy to build

L. He, H. Zhang, F. Zhang, W. Zhang, X. Zhang
Key Laboratory of Advanced Optoelectronic Quantum Architecture and Measurements of Ministry of Education
Beijing Key Laboratory of Nanophotonics and Ultrafine Optoelectronic Systems
School of Physics
Beijing Institute of Technology
Beijing 100081, China
E-mail: zhangxd@bit.edu.cn

D. Liu, X. Feng, Y. Huang, K. Cui, F. Liu, W. Zhang
Frontier Science Center for Quantum Information
Beijing National Research Center for Information Science and Technology (BNRist)
Electronic Engineering Department
Tsinghua University
Beijing 100084, China
E-mail: zwei@tsinghua.edu.cn

Y. Huang, W. Zhang
Beijing Academy of Quantum Information Sciences
Beijing 100193, China

The ORCID identification number(s) for the author(s) of this article can be found under https://doi.org/10.1002/adma.202311611

DOI: 10.1002/adma.202311611

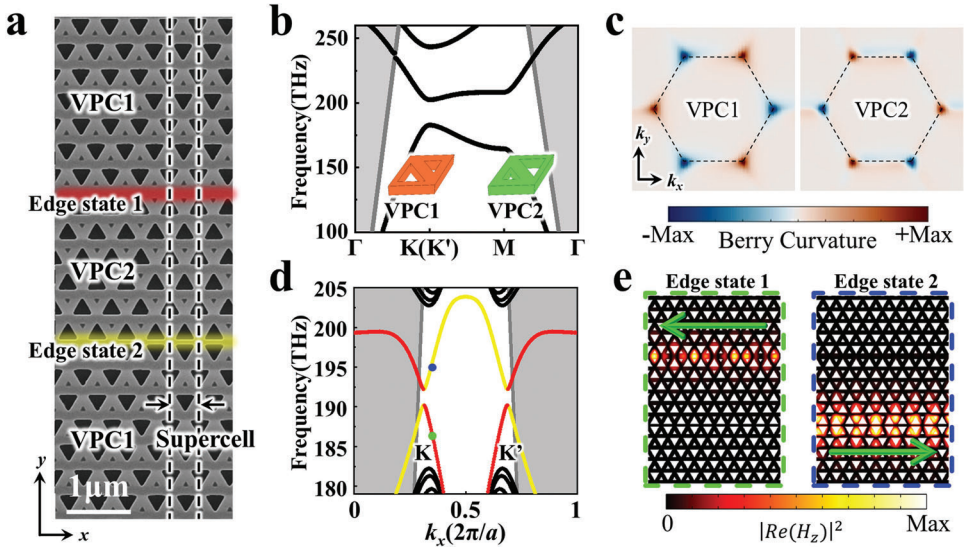

Figure 1. Topological valley photonic crystals. a) The SEM image of the valley photonic crystal slabs, which includes two kinds of valley photonic crystals, VPC1 and VPC2. The lattice constant is 450 nm. There are two triangular air holes in the unit cells and the sides of them are $d_1 = 120$ nm and $d_2 = 300$ nm ($d_1 = 300$ nm and $d_2 = 120$ nm) for VPC1 (VPC2). The dashed line delineates the boundary of the sandwich-type supercell consisting of VPC1, VPC2, and VPC1. There are two edge states (1 and 2), marked as red and yellow lines, at the boundaries of VPC1|VPC2 and VPC2|VPC1. b) The TE-mode band structure of the unit cell for VPC1 (VPC2), marked as black lines. The gray regions cover the leak mode (not shown) above the light cone. c) Berry curvature distribution of the first band of VPC1 and VPC2. The black dashed line represents the first Brillouin zone. d) The topological band structure of the supercell. The red (yellow) lines represent edge state modes at the boundaries of edge state 1 (2). The black lines represent the bulk bands. The gray line represents the light cone line. e) The simulation results of the norm of the real part of the magnetic field distribution for the edge state 1 (green dashed box) and 2 (blue dashed box) with the wave vector being $k_x = 0.7\pi/a$. They correspond to green and blue points in (d). The green arrows represent the direction of propagation of the edge state 1 and 2.

topologically protected quantum gates. For example, to realize CNOT gates, we need to build a topologically protected 2 × 2 beam splitter (BS) with an unbalanced splitting ratio (33:67). At present, how to build such devices is an outstanding question because the topological edge states with chirality cannot be directly used to realize the quantum gate-required 2 × 2 BS.

In this work, based on designing and fabricating topologically protected contradirectional couplers by using topological valley photonic crystals (TVPCs), the topologically protected 2 × 2 BS with an arbitrary splitting ratio has been realized. And then, the topologically protected Hadamard and CNOT gates have been constructed on silicon (Si) photonic platforms. Importantly, these quantum logic gates show a certain degree of tolerance against manufacturing defects and a low loss (experimentally −3 dB). It is expected that our designed topologically protected quantum gates possess great potential applications in future quantum computing and signal processing.

2. Topologically Protected Contradirectional Couplers

We consider a sandwich-type TVPCs structure on the silicon-on-insulator (SOI) platform with a 220 nm thick Si layer. The scanning electron microscopy (SEM) image of the fabricated sample is shown in **Figure** 1a. The detailed structure parameters and fabrication process are described in Methods. The transverse-electric-like (TE-like) band structures for VPC1 and VPC2 are calculated and plotted in Figure 1b. We can see that the bandgap appears at K(K') point at both structures. Although the band dispersions for VPC1 and VPC2 are exactly the same, they have different topological properties. To illustrate this effect, we calculate profiles of Berry curvature for the first band of VPC1 and VPC2 in momentum space, as shown in Figure 1c. The Berry curvatures with opposite signs appear at K(K') points, manifesting the different valley topologies for two structures.

To further illustrate the nontrivial topology of the system, we plot the dispersion relation of the supercell structure in Figure 1d. It is clearly seen that two edge states (labeled by '1' and '2') appear in the topological bandgap and they have the negative and positive group velocities at K valley, respectively. The opened gap between two edge states is resulting from the finite size effect, which can trigger the coupling between two edge states. Figure 1e presents spatial distributions of two edge states, which are located at opposite domain walls of the system. In addition, it is clearly observed that these two edge states possess different propagation directions.

By utilizing the unique properties of topological edge states, the topological contradirectional coupler (topo-CDC) can be designed. Compared to the traditional directional coupler, the topo-CDC is composed of a sandwich-type TVPC structure and has four ports labeled as Ports 1–4. The SEM image of the fabricated topo-CDC is shown in **Figure** 2a. When injecting light into Port 1 with the wavelength locating at the gap of two edge states, the signal can propagate into Port 3 due to the coupling between the two edge states. When the wavelength of the input light matches the right-propagated edge state 2, the input light can leave from Port 2. It is important to note that the case of inputting light from Port 2 is similar to that from Port 1 due to the mirror symmetry

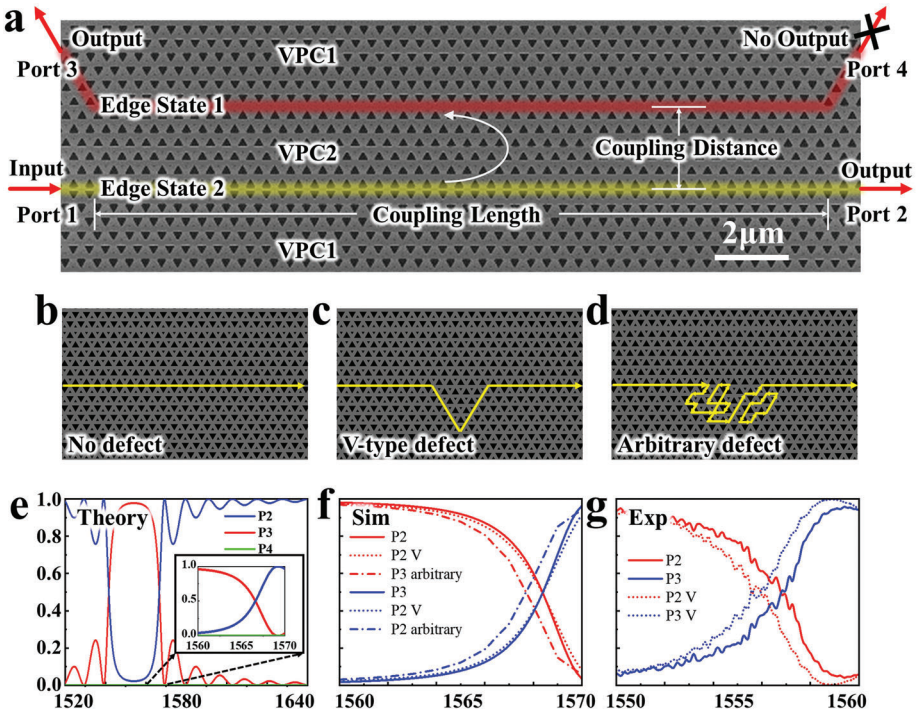

Figure 2. Topologically protected contradirectional coupler. a) The SEM image of the contradirectional coupler based on Si valley photonic crystal slabs. The topo-CDC with b) no defect, c) V-type defect, and d) arbitrary shape defect. e) The theoretical normalized transmission spectra according to the CMT theory. The f) simulation and g) experiment results of the topo-CDC with various defects.

of the CDC. The output light at Port 4 is forbidden because edge modes in the topo-CDC are locked at K valley and cannot transition to the modes at K' valley, even though some disorders exist. This is the most significant difference between the topo-CDC and trivial CDC.[65]

To demonstrate the topological protection of the topo-CDC, we construct three structures with no defect, a V-type defect, and an arbitrary shape defect, as shown in Figure 2b–d. Figure 2e shows the theoretical transmissivities for Ports 2–4, which are calculated using coupling mode theory (CMT). The detailed calculation process can be found in Section S1 of Supporting Information. The output powers of Ports 2 and 3 are equal (50:50) at the wavelength of 1565 nm, while the output power at Port 4 is close to zero. This indicates that the topo-CDC can perform the function of a 2×2 beam splitter with an equal beam splitting ratio. By adjusting the wavelength of input light or employing thermally tuned control, the topo-CDC can also realize the 2×2 beam splitter with other splitting ratios. Full-wave numerical simulations (plotted in Figure 2f) further demonstrate the good performance of the designed topo-CDC. We can conclude that the topo-CDC shows a good performance to achieve the function of balanced beam splitting against some defects which are not mixing valleys.

We tested whether our fabricated structure can implement the function of the topo-CDC by measuring the normalized output power of Ports 2–4 (Figure 2g), obtaining a splitting ratio of 33:67 between Ports 2 and 3 at the specific wavelength (≈1555 nm), and close to zero output power at Port 4. The full spectrum of the topo-CDC is in Section S2 of Supporting Information, and our experiment results match simulations, indicating good performance. In addition, we also measure a low insertion loss of the topo-CDC, about −3 dB (see Section S3.2 of Supporting Information).

The key feature of the topo-CDC is the immunity to different defects. We tested this feature by considering waveguide bending. The corresponding numerical and experimental results for the normalized transmission spectra are plotted as dashed lines in Figure 2f,g, respectively. Comparing them with those without bending, we found that they are basically the same. Similar results can be obtained for other kinds of bending (see Section S3 of Supporting Information). This indicates perfect topological protection against waveguide bending. For air-hole disorder, simulation results show the topo-CDC's disorder tolerance is more than one order of magnitude compared to trivial designs. Additionally, our device possesses the robustness against backscattering (see Section S4, Supporting Information, for details).

3. Topologically Protected CNOT Gates

We can design topologically protected quantum logic devices by using topo-CDCs because they can perform the function of 2×2 BS with any splitting ratio. If the ratio is 33:67 (50:50), the BS can be used to construct the CNOT (Hadamard) gate. As shown in Figure 2d–g, the black dashed lines mark the wavelength at the 33:67 ratio is realized. Although many topological BSs[60,66] have been reported, they are all 1×2 BSs due to the chirality of the topological edge state and thus cannot construct quantum logic gates. Detailed discussions are in Section S5 in the Supporting Information.

Following the linear optical scheme,[8] we can construct the topologically protected two-qubit CNOT gates by suitably

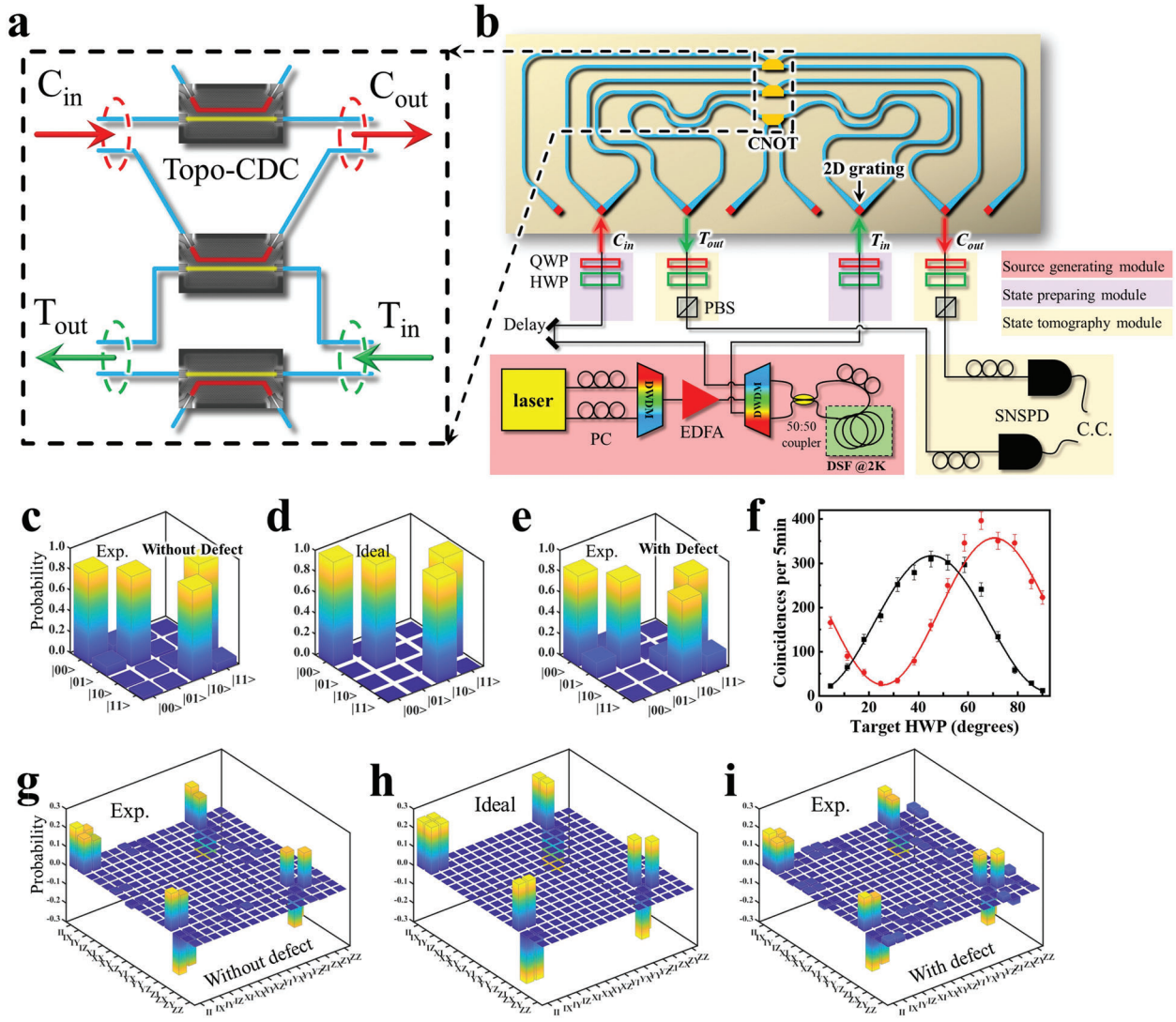

Figure 3. Topologically protected CNOT gate. a) The scheme of the CNOT gate constructed by three topo-CDCs. b) Schematic of the topologically protected CNOT gate on Si chip and its experimental setup. PC: polarization controller. DWDM: cascaded dense wavelength division multiplexer. EDFA: Erbium doped fiber amplifier. DSF: dispersion-shifted fiber. C.C.: coincidence counting. The experimental matrices of truth table for CNOT gate c) without and e) with the disorder. The experimental fidelities are $F = 0.9380 \pm 0.0051$ and $F = 0.9076 \pm 0.0058$, respectively. d) The corresponding ideal matrix of truth table for the CNOT gate under the ZZ-basis. f) Coincidence fringes under nonorthogonal bases. The control analyzer is set to pass the $\frac{1}{\sqrt{2}}(|H\rangle+|V\rangle)$ (red dots) and $|H\rangle$ (black dots) with the input state being $\frac{1}{\sqrt{2}}(|0\rangle+|1\rangle)_c|1\rangle_t$. The red and black lines fitting sine curves. Error bars come from the Poisson statistics of photon counts. The quantum process tomography of CNOT gate for the experimental results g) without and i) with the disorder. Their process fidelities F_{CNOT} are 0.9053 ± 0.0046 and 0.8812 ± 0.0057, respectively. h) The ideal quantum process tomography of the CNOT gate.

combining three topologically protected 33:67 BSs in parallel, as shown in **Figure** 3a. Each waveguide pair labeled by C_{in}, C_{out}, T_{in}, and T_{out}, respectively, path-encodes the control and target photons and connects to two 33:67 BSs, satisfying the CNOT gate requirement. The detailed discussions can be seen in Section S6 of the Supporting Information.

According to the above scheme, we fabricate such a CNOT gate on the SOI chip. The schematic diagram for the experimental setup is presented in Figure 3b. Here, the frequency-degenerated photon pairs are well generated. We carry out an experimental test and achieve a net visibility of 99.61% in the Hong-Ou-Mandel interference[67] dip, which indicates a high-quality two-photon source (see Section S7, Supporting Information, for details).

Then, the photons are encoded in polarization-based logic qubits in free space. The polarization states of photons can be arbitrarily adjusted by the state preparing module, which consists of a set of wave plates, the quarter-wave plate (QWP), and the half-wave plate (HWP). To implement the CNOT gate, the measurement of operation under ZZ-basis is considered. The control (target) qubits are defined as $|0\rangle_c \equiv |H\rangle$ and $|1\rangle_c \equiv |V\rangle$ ($|0\rangle_t \equiv \frac{1}{\sqrt{2}}(|H\rangle + |V\rangle)$ and $|1\rangle_t \equiv \frac{1}{\sqrt{2}}(|H\rangle - |V\rangle)$). The encoded

photons are injected into the chip with a 2D grating coupler, which transforms the polarization-encoded photons in free space into path-encoded photons within chips. With the two-photon interference happening at the topo-CDCs, the CNOT function is carried out. In this case, the output quantum qubits can be detected by the state tomography module with HWPs, QWPs, polarization beam splitters (PBSs), and fiber-coupled superconducting nanowire single-photon detectors (SNSPDs). The details about the experimental setup can be found in Section S1 in the Supporting Information.

The function of the CNOT gate is tested by analyzing the measured two-photon coincidence counts. The output state related to four different input states $|00\rangle_{ct}$, $|01\rangle_{ct}$, $|10\rangle_{ct}$, and $|11\rangle_{ct}$ is measured to characterize the operation of the designed CNOT gate. Measured results for the truth table of the CNOT gate are presented in Figure 3c. The corresponding ideal result is shown in Figure 3d. By comparison, we find that the experimental result is in a good agreement with theory, indicating a nice performance of the CNOT gate. The small discrepancy between the experimental and ideal fidelities is mainly attributed to the instability of the polarization of control and target photons in the fiber and the imperfect BS ratio for the 33:67 BSs. To further quantify the experimental result, we calculate the averaged transformation fidelity of CNOT gate, which is expressed as $F = Tr(\sqrt{\sqrt{M_{\text{th}}}M_{\text{exp}}\sqrt{M_{\text{th}}}})$ with M_{th} and M_{exp} being the theoretical and experimental matrixes of truth table for the CNOT gate. An extremely high-valued fidelity with $F = 0.9380 \pm 0.0051$ clearly confirms that our implementation on the quantum CNOT function has a good performance.

The designed CNOT gate based on the topo-CDC possesses the feature of topological protections and is also robust against a certain degree of defects. The measured truth table of the CNOT gate in the system with disorders is shown in Figure 3e, where a V-type waveguide bending is taken, and the corresponding fidelity equals to $F = 0.9076 \pm 0.0058$. We note that only a little difference exists between the cases with or without the disorder, meaning that our designed CNOT gate possesses a strong error tolerance against disorders. As for the other type of disorders, our quantitative analysis indicates that the designed quantum gate also has good error-tolerance properties. Detailed discussion is given in Section S3.2.2 in the Supporting Information.

The CNOT gate is vital for creating entangled two-photon quantum states, and our topologically protected CNOT gate can robustly achieve this. Our focus is on generating maximally entangled Bell state $\Psi^- = \frac{1}{\sqrt{2}}(|01\rangle_{ct} - |10\rangle_{ct})$ from a separable state $\frac{1}{\sqrt{2}}(|0\rangle_c - |1\rangle_c)|1\rangle_t$. For this purpose, the control and target quantum states with the forms of $\frac{1}{\sqrt{2}}(|H\rangle - |V\rangle)$ and $\frac{1}{\sqrt{2}}(|H\rangle - |V\rangle)$ are injected into the CNOT gate. The entangling property of output two-photon states can be verified by measuring conditional fringe visibilities.[68] In this case, the measured coincident-photon-count rates as a function of the rotation angle for HWP in the target analyzer are presented in Figure 3f. The visibilities ($v = (C_{\text{max}} - C_{\text{min}})/(C_{\text{max}} + C_{\text{min}})$, C_{max}, and C_{min} correspond to the maximum and minimum values of the measured coincident-photon-count rates) for the fitted curves of coincident-photon-count rates are calculated as 93.57% and 86.90% (>70.7%), indicating our CNOT gate is efficient at generating entanglement.

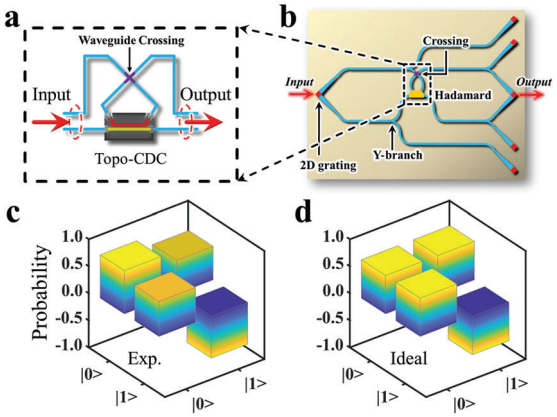

Figure 4. Topologically protected Hadamard gate. a) The scheme of the Hadamard gate, which is constructed by a topo-CDC and a waveguide crossing. b) Schematic of the topologically protected Hadamard gate on Si chip. There are four Y-branch structures and one waveguide crossing on the chip. Except for the input and output gratings, there are also four additional gratings to help calibrate the polarization states of input and output photons. c) The experimental matrix of the Hadamard gate. d) The ideal matrix of the Hadamard gate.

Furthermore, we also perform the quantum process tomography to fully characterize the topologically protected CNOT gate. For a generic quantum process ζ acting on a 2-qubit density matrix β, we always have the expression of $\zeta(\beta) = \sum_{m,n=1}^{15} \chi_{mn}\hat{A}_m\beta\hat{A}_n^{\dagger}$, where the operator $\hat{A}_m$ ($\hat{A}_n$) is defined as the tensor product of Pauli matrices $\{\hat{A}_m \equiv \sigma_i \otimes \sigma_j\}$, $i, j = 0,...,3$, $m = 0,...,15$. The process matrix χ_{mn} contains all information for the quantum process. The experimentally reconstructed process matrix is plotted in Figure 3g, where a good consistent exists between the measured process matrix and the ideal process matrix (labeled by χ_{CNOT} shown in Figure 3h). Using the definition of process fidelity[69,70] $F_{\text{CNOT}} = Tr[\sqrt{\sqrt{\chi_{\text{exp}}}\chi_{\text{CNOT}}\sqrt{\chi_{\text{exp}}}}]^2/Tr[\chi_{\text{exp}}]Tr[\chi_{\text{CNOT}}]$, we obtain $F_{\text{CNOT}} = 0.9053 \pm 0.0046$, which shows a high-performance efficiency of the fabricated CNOT gate.

To demonstrate the topological protection of CNOT gate, we experimentally reconstruct the process matrix of the CNOT gate in the system sustaining a V-type waveguide bending, as shown in Figure 3i. The associated fidelity equals to $F_{\text{CNOT}} = 0.8812 \pm 0.0057$. Those experimental results indicate that the implementation of logical functions by the topological CNOT gate is nearly unaffected under the influence of bending disorder.

4. Topologically Protected Hadamard Gate

Except for the robust CNOT gate, the topologically protected Hadamard gate can also be realized by topo-CDC ($T = R = 50\%$). The scheme of Hadamard gate is shown in **Figure** 4a. The input and output photons are path-encoded in each waveguide pair and a suitably designed waveguide crossing is applied to put the input or output waveguides together. Similar to the CNOT gate, the 2D gratings are also used to transform the polarization-encoded photons in free space into path-encoded photons in chips.

The fabricated Hadamard gate on the SOI chip is presented in Figure 4b. When the polarization-encoded single-photon state

is injected into the chip assisted by the input 2D grating, the single-photon state possesses the path-encoded property of two input waveguides, which connect to Ports 1 and 4 of the topo-CDC. After the single-photon interference implemented by the Hadamard gate, the transformed single-photon state leaves away from output waveguides and is then coupled into the fiber by output 2D gratings. Going outside from the chip, the single-qubit tomography of the Hadamard gate is performed by HWPs, QWPs, and PBSs (similar to the case of CNOT gate).

In experiments, six different input single-photon states, including $|0\rangle$, $|1\rangle$, $\frac{1}{\sqrt{2}}(|0\rangle+|1\rangle)$, $\frac{1}{\sqrt{2}}(|0\rangle-|1\rangle)$, $\frac{1}{\sqrt{2}}(|0\rangle+i|1\rangle)$, and $\frac{1}{\sqrt{2}}(|0\rangle-i|1\rangle)$, are generated and injected into the Hadamard gate, where $|0\rangle$ and $|1\rangle$ correspond to the free-space polarization state $|H\rangle$ and $|V\rangle$ of the single photon. After going through the Hadamard gate, the output quantum states are projected to the basis composed of the six input states. In this case, the projection probabilities of these output states for all input states are recorded in a 6 × 6 matrix. Based on these measurement data, we retrieve the experimental transformation matrix with $|0\rangle$ and $|1\rangle$ bases, as shown in Figure 4c. It is clearly seen that the input states of $|0\rangle$ and $|1\rangle$ are successfully transformed into $\frac{1}{\sqrt{2}}(|0\rangle+|1\rangle)$ and $\frac{1}{\sqrt{2}}(|0\rangle-|1\rangle)$, respectively. The experimental matrix of the Hadamard operation is very close to the ideal counterpart, which is shown in Figure 4d. For quantitatively characterizing the Hadamard gate, we calculate its fidelity[22] F_{H} being 0.959, which is defined as $F_H = |\langle\phi|M_{\mathrm{th}}M_{\mathrm{exp}}|\phi\rangle|^2$. Here, $|\phi\rangle$ is the quantum state $|0\rangle$ or $|1\rangle$. Such a high fidelity further indicates that the function of our designed Hadamard gate is well implemented. Additionally, our Hadamard gate can also be combined with the CNOT on one chip. In this way, more complex quantum circuits can be implemented. See Section S8 in the Supporting Information for details.

5. Summary

In summary, we have theoretically designed and experimentally fabricated topo-CDCs based on valley photonic crystals. Our designed scheme of topo-CDC solves the problem that the previous topological BS cannot perform the function of 2 × 2 BS with an arbitrary splitting ratio. Importantly, the topo-CDC possesses high-performance efficiencies and the robustness against a certain degree of defects. Based on our designed topo-CDC, the major quantum logic gates, including CNOT and Hadamard gates, have been realized on the silicon photonic platform. The high-performance efficiencies and a certain degree of robustness of these topologically protected quantum gates have also been demonstrated. This work provides novel designs for on-chip integrated quantum information processing, which is expected to solve the problem of robustness in optical quantum computing and signal processing.

6. Methods

6.1. Structure Parameters

The structure is composed of two kinds of TVPCs, which are named as VPC1 and VPC2, respectively. The environmental background is air and the refractive index of Si is taken as 3.48. Two domain walls are marked by red and yellow lines, respectively. Enlarged views of their unit cells are shown in the inset of Figure 1b. There are two different triangular air holes in each unit with the period being a = 450 nm. It is worth noting that edge lengths of two triangle air holes, which are d_1 = 300 nm (120 nm) and d_2 = 120 nm (300 nm) for VPC1 (VPC2), are different to break the inversion symmetry.

In the calculation of the topological band structure of the supercell, the supercell is periodic in the x direction and has a finite length (20 a) in the y direction.

In the topo-CDC, there is a rectangular coupling region between two domain walls, where the coupling distance and length are set as $3\sqrt{3}\,a$ and 50 a, respectively.

6.2. Sample Fabrication

First, the photonic crystal slabs were fabricated using electron beam lithography, followed by dry etching. The substrate was a silicon-on-insulator wafer with a 220 nm thick top Si layer. ZEP-520A e-beam resist was first spun-coated on the substrate for exposure and resist patterns were formed after e-beam lithography and development. Then these resist patterns were transferred to the top Si layer using inductively coupled plasma etching in SF_6 and CHF_3 gases atmosphere, with ZEP520A used as an etching mask. The etching depth for quantum gates and waveguides is 220 nm.

In the second step, the SiO_2 under the photonic crystal slab was removed by the wet etching process. We used a patterned photoresist (S1813) as a mask for the wet etching. S1813 photoresist was first spun onto the sample and resist patterns were formed after ultraviolet lithography and development. Next, the patterned photoresist was hardbaked on a hotplate for 60 min at 115 °C. Then the sample was rinsed in a buffered oxide etch, and the SiO_2 under the photonic crystal slab was etched away with the patterned photoresist used as etching mask. Finally, the photoresist was stripped away with acetone, followed by O_2 plasma treatment to clean the residual photoresist thoroughly.

7. Experimental Section

The Quantum Source Generating: In experiments, two continuous wave mono-color pump lights (with frequencies being ω_1 and ω_3) are combined and injected into the region for generating the quantum source (highlighted by a red box), which is constructed by a Sagnac loop in the dispersion-shifted fibers. The fiber is cooled down to about 2K for suppressing the Raman noise. Additionally, the cascaded dense wavelength division multiplexers (cascaded DWDMs) are used to remove the residual pump photons. In this case, two photons with the frequency being ω_2 ($2\omega_2 = \omega_1 + \omega_3$) are generated while the photons of ω_1 and ω_3 are annihilated in the spontaneous four-wave mixing process.

The Coupling between the Free Space and the On-Chip Waveguide: Two-photon quantum states are coupled into optical fibers by 2D output gratings. In this case, the photons away from the chip can retransform into polarization-encoded photons in free space.

The Delay Lines: For obtaining the best interference effect, the delay line was also adjusted carefully to maximize the temporal overlap between control and target photons. Based on such a setup, the function of CNOT gate can be tested by analyzing the measured two-photon coincidence counts.

Optical Apparatus: The continuous wave laser (keysight N7714A) is employed to generate the pump light in the experiment and the frequencies of the two pump lights are 193.9 and 194.3 THz, respectively. The incident laser is first coupled to the single mode fibers (SMFs), is combined by the DWDMs, and injected into the chip by the fiber array. Next, stimulating spontaneous four-wave mixing in the dispersion-shifted fiber of the temperature being 2K, where the frequency-degenerate photon pairs (194.1 THz) are generated. Four sets of computer-controlled wave-plane rotators are used for generating any biphotonic state and projecting it to any measurement basis. The output photons from the chip coupled to the SMFs of the fiber array, went through the DWDMs (filter out the pump light), and are counted by the SNSPDs. The efficiencies of single photon detectors are about ≈50% and dark count rates are about ≈100 Hz. Finally, we perform a coincidence measurement between the two photons.

Supporting Information

Supporting Information is available from the Wiley Online Library or from the author.

Acknowledgements

The authors would like to thank Hao Li and Lixing You from Shanghai Institute of Microsystem and Information Technology, Chinese Academy of Sciences, China for their support on the SNSPDs used in this work. This work was supported by the National key R&D Program of China (2022YFA1404904 and 2018YFB2200400), National Natural Science Foundation of China (No. 12234004).

Conflict of Interest

The authors declare no conflict of interest.

Author Contributions

L.H. finished the theoretical scheme and designed the experiments. L.H. finished experiments with the help of D.L., H.Z., F.Z., X.F., F.L., K.C. under the supervision of W.Z. and Y.D.H. L.H. and X.D.Z. wrote the paper with the help of W.Z. and W.X.Z. X.D.Z. initiated and designed this research project.

Data Availability Statement

The data that support the findings of this study are available from the corresponding author upon reasonable request.

Keywords

quantum circuit, quantum gate, topological protection, valley photonic crystals

Received: November 3, 2023
Revised: February 23, 2024
Published online: March 20, 2024

[1] M. A. Nielsen, I. L. Chuang, *Quantum Computation and Quantum Information*, Cambridge Univ. Press, Cambridge **2000**.
[2] T. D. Ladd, F. Jelezko, R. Laflamme, Y. Nakamura, C. Monroe, J. L. O'Brien, *Nature* **2010**, *464*, 45.
[3] E. Knill, R. Laflamme, G. J. Milburn, *Nature* **2001**, *409*, 46.
[4] D. Gottesman, I. L. Chuang, *Nature* **1999**, *402*, 390.
[5] A. Barenco, C. H. Bennett, R. Cleve, D. P. DiVincenzo, N. Margolus, P. Shor, T. Sleator, J. A. Smolin, H. Weinfurter, *Phys. Rev. A* **1995**, *52*, 3457.
[6] N. J. Cerf, C. Adami, P. G. Kwiat, *Phys. Rev. A* **1998**, *7*, R1477.
[7] H. F. Hofmann, S. Takeuchi, *Phys. Rev. A* **2002**, *66*, 024308.
[8] R. Okamoto, H. F. Hofmann, S. Takeuchi, K. Sasaki, *Phys. Rev. Lett.* **2005**, *95*, 210506.
[9] A. Politi, M. J. Cryan, J. G. Rarity, S. Yu, J. L. O'brien, *Science* **2008**, *320*, 646.
[10] D. E. Browne, T. Rudolph, *Phys. Rev. Lett.* **2005**, *95*, 010501.
[11] A. Crespi, R. Ramponi, R. Osellame, L. Sansoni, I. Bongioanni, F. Sciarrino, G. Vallone, P. Mataloni, *Nat. Commun.* **2011**, *2*, 566.
[12] B. Hacker, S. Welte, G. Rempe, S. Ritter, *Nature* **2016**, *536*, 193.
[13] S. M. Wang, Q. Q. Cheng, Y. X. Gong, P. Xu, C. Sun, L. Li, T. Li, S. N. Zhu, *Nat. Commun.* **2016**, *7*, 11490.
[14] J. Zeuner, A. N. Sharma, M. Tillmann, R. Heilmann, M. Gräfe, A. Moqanaki, A. Szameit, P. Walther, *npj Quantum Inf.* **2018**, *4*, 13.
[15] K. S. Chou, J. Z. Blumoff, C. S. Wang, P. C. Reinhold, C. J. Axline, Y. Y. Gao, L. Frunzio, M. H. Devoret, L. Jiang, R. J. Schoelkopf, *Nature* **2018**, *561*, 368.
[16] M. Zhang, L. Feng, M. Li, Y. Chen, L. Zhang, D. He, G. Guo, G. Guo, X. Ren, D. Dai, *Phys. Rev. Lett.* **2021**, *126*, 130501.
[17] N. K. Langford, T. J. Weinhold, R. Prevedel, K. J. Resch, A. Gilchrist, J. L. O'Brien, G. J. Pryde, A. G. White, *Phys. Rev. Lett.* **2005**, *95*, 210504.
[18] M. Fiorentino, F. N. C. Wong, *Phys. Rev. Lett.* **2004**, *93*, 070502.
[19] J. J. Vartiainen, M. Möttönen, M. M. Salomaa, *Phys. Rev. Lett.* **2004**, *92*, 177902.
[20] G. Vidal, C. M. Dawson, *Phys. Rev. A* **2004**, *69*, 010301.
[21] M. Heuck, K. Jacobs, D. R. Englund, *Phys. Rev. Lett.* **2020**, *124*, 160501.
[22] R. Heilmann, M. Gräfe, S. Nolte, A. Szameit, *Sci. Rep.* **2014**, *4*, 4118.
[23] J. L. O'Brien, A. Furusawa, J. Vučković, *Nat. Photonics* **2009**, *3*, 687.
[24] X. Qiang, X. Zhou, J. Wang, C. M. Wilkes, T. Loke, S. O'Gara, L. Kling, G. D. Marshall, R. Santagati, T. C. Ralph, J. B. Wang, J. L. O'Brien, M. G. Thompson, J. C. F. Matthews, *Nat. Photonics* **2018**, *12*, 534.
[25] J. Wang, F. Sciarrino, A. Laing, M. G. Thompson, *Nat. Photonics* **2020**, *14*, 273.
[26] Y.-J. Cai, M. Li, X.-F. Ren, C.-L. Zou, X. Xiong, H.-L. Lei, B.-H. Liu, G.-P. Guo, G.-C. Guo, *Phys. Rev.* **2014**, *2*, 014004.
[27] E. Knill, *Nature* **2005**, *434*, 39.
[28] D. Gottesman, *Phys. Rev. A* **1998**, *57*, 127.
[29] A. M. Steane, *Nature* **1999**, *399*, 124.
[30] X.-C. Yao, T.-X. Wang, H.-Z. Chen, W.-B. Gao, A. G. Fowler, R. Raussendorf, Z.-B. Chen, N.-L. Liu, C.-Y. Lu, Y.-J. Deng, Y.-A. Chen, J.-W. Pan, *Nature* **2012**, *482*, 489.
[31] A. Paetznick, B. W. Reichardt, *Phys. Rev. Lett.* **2013**, *111*, 090505.
[32] D. Nigg, M. Müller, E. A. Martinez, P. Schindler, M. Hennrich, T. Monz, M. A. Martin-Delgado, R. Blatt, *Science* **2014**, *345*, 302.
[33] N. M. Linke, M. Gutierrez, K. A. Landsman, C. Figgatt, S. Debnath, K. R. Brown, C. Monroe, *Sci. Adv.* **2017**, *3*, 1701074.
[34] S. Takeda, A. Furusawa, *APL Photonics* **2019**, *4*, 060902.
[35] S. Omkar, Y. S. Teo, H. Jeong, *Phys. Rev. Lett.* **2020**, *125*, 060501.
[36] L. Egan, D. M. Debroy, C. Noel, A. Risinger, D. Zhu, D. Biswas, M. Newman, M. Li, K. R. Brown, M. Cetina, C. Monroe, *Nature* **2021**, *598*, 281.
[37] F. D. M. Haldane, S. Raghu, *Phys. Rev. Lett.* **2008**, *100*, 013904.
[38] G. J. Tang, X. T. He, F. L. Shi, J. W. Liu, X. D. Chen, J. W. Dong, *Laser Photonics Rev.* **2022**, *16*, 2100300.
[39] Z. Wang, Y. Chong, J. D. Joannopoulos, M. Soljačić, *Nature* **2009**, *461*, 772.
[40] J. Ma, X. Xi, X. Sun, *Adv. Mater.* **2021**, *33*, 2006521.

[41] A. B. Khanikaev, S. H. Mousavi, W. K. Tse, M. Kargarian, A. H. MacDonald, G. Shvets, *Nat. Mater.* **2013**, *12*, 233.
[42] L. H. Wu, X. Hu, *Phys. Rev. Lett.* **2015**, *114*, 223901.
[43] Y. Hou, S. Yuan, G. Zhu, B. You, Y. Xu, W. Jiang, H. C. Shum, P. W. T. Pong, C.-H. Chen, L. Wang, *Adv. Mater.* **2023**, *35*, 2209004.
[44] T. Ma, G. Shvets, *New J. Phys.* **2016**, *18*, 025012.
[45] Y. Yang, Y. F. Xu, T. Xu, H. X. Wang, J. H. Jiang, X. Hu, Z. H. Hang, *Phys. Rev. Lett.* **2018**, *120*, 217401.
[46] M. I. Shalaev, W. Walasik, A. Xu, Y. Tsukernik, N. M. Litchinitser, *Nat. Nanotechnol.* **2019**, *14*, 31.
[47] T. Ozawa, H. M. Price, A. Amo, N. Goldman, M. Hafezi, L. Lu, M. C. Rechtsman, D. Schuster, J. Simon, O. Zilberberg, I. Carusotto, *Rev. Mod. Phys.* **2019**, *91*, 015006.
[48] X. T. He, E. T. Liang, J. J. Yuan, H. Y. Qiu, X. D. Chen, F. L. Zhao, J. W. Dong, *Nat. Commun.* **2019**, *10*, 872.
[49] Y. Wang, Y. H. Lu, J. Gao, K. Sun, Z. Q. Jiao, H. Tang, X. M. Jin, *Adv. Mater.* **2019**, *31*, 1905624.
[50] Y. Yang, Y. Yamagami, X. Yu, P. Pitchappa, J. Webber, B. Zhang, M. Fujita, T. Nagatsuma, R. Singh, *Nat. Photonics* **2020**, *14*, 446.
[51] A. Kumar, M. Gupta, P. Pitchappa, T. C. Tan, U. Chattopadhyay, G. Ducournau, N. Wang, Y. Chong, R. Singh, *Adv. Mater.* **2022**, *34*, 2202370.
[52] M. C. Rechtsman, Y. Plotnik, J. M. Zeuner, D. Song, Z. Chen, A. Szameit, M. Segev, *Phys. Rev. Lett.* **2013**, *111*, 103901.
[53] J. Guglielmon, M. C. Rechtsman, *Phys. Rev. Lett.* **2019**, *122*, 153904.
[54] C. A. Rosiek, G. Arregui, A. Vladimirova, M. Albrechtsen, B. Vosoughi Lahijani, R. E. Christiansen, S. Stobbe, *Nat. Photonics* **2023**, *17*, 386.
[55] S. Xu, Y. Wang, R. Agarwal, *Phys. Rev. Lett.* **2023**, *131*, 053802.
[56] S. Barik, A. Karasahin, C. Flower, T. Cai, H. Miyake, W. DeGottardi, M. Hafezi, E. Waks, *Science* **2018**, *359*, 666.
[57] A. Blanco-Redondo, B. Bell, D. Oren, B. J. Eggleton, M. Segev, *Science* **2018**, *362*, 568.
[58] S. Mittal, E. A. Goldschmidt, M. Hafezi, *Nature* **2018**, *561*, 502.
[59] S. Mittal, V. V. Orre, E. A. Goldschmidt, M. Hafezi, *Nat. Photonics* **2021**, *15*, 542.
[60] Y. Chen, X.-T. He, Y.-J. Cheng, H.-Y. Qiu, L.-T. Feng, M. Zhang, D.-X. Dai, G.-C. Guo, J.-W. Dong, X.-F. Ren, *Phys. Rev. Lett.* **2021**, *126*, 230503.
[61] W. Yao, D. Xiao, Q. Niu, *Phys. Rev. B* **2008**, *77*, 235406.
[62] J. Noh, S. Huang, K. P. Chen, M. C. Rechtsman, *Phys. Rev. Lett.* **2018**, *120*, 063902.
[63] X.-D. Chen, F.-L. Zhao, M. Chen, J.-W. Dong, *Phys. Rev. B* **2017**, *96*, 020202.
[64] T. Dai, Y. Ao, J. Bao, J. Mao, Y. Chi, Z. Fu, Y. You, X. Chen, C. Zhai, B. Tang, Y. Yang, Z. Li, L. Yuan, F. Gao, X. Lin, M. G. Thompson, J. L. O'Brien, Y. Li, X. Hu, Q. Gong, J. Wang, *Nat. Photonics* **2022**, *16*, 248.
[65] Z. Xu, J. Wang, Q. He, L. Cao, P. Su, G. Jin, *Opt. Express* **2005**, *13*, 5608.
[66] L. He, H. Y. Ji, Y. J. Wang, X. D. Zhang, *Opt. Express* **2020**, *28*, 34015.
[67] C. K. Hong, Z. Y. Ou, L. Mandel, *Phys. Rev. Lett.* **1987**, *59*, 2044.
[68] C. H. Bennett, G. Brassard, S. Popescu, B. Schumacher, J. A. Smolin, W. K. Wootters, *Phys. Rev. Lett.* **1996**, *76*, 722.
[69] J. L. O'Brien, G. J. Pryde, A. Gilchrist, D. F. V. James, N. K. Langford, T. C. Ralph, A. G. White, *Phys. Rev. Lett.* **2004**, *93*, 080502.
[70] L. Sansoni, F. Sciarrino, G. Vallone, P. Mataloni, A. Crespi, R. Ramponi, R. Osellame, *Phys. Rev. Lett.* **2010**, *105*, 200503.